

Kinematics and line strength indices in the halos of the Coma Brightest Cluster Galaxies NGC 4874 and NGC 4889 [★]

L. Coccato¹, M. Arnaboldi^{2,3}, O. Gerhard¹, K. C. Freeman⁴, G. Ventimiglia^{1,2}, and N. Yasuda⁵

¹ Max-Planck-Institut für Extraterrestrische Physik, Giessenbachstraße 1, D-85741 Garching bei München, Germany.

² European Southern Observatory, Karl-Schwarzschild-Straße 2, 85748 Garching bei München, Germany.

³ INAF, Osservatorio Astronomico di Pino Torinese, I-10025 Pino Torinese, Italy.

⁴ Research School of Astronomy & Astrophysics, ANU, Canberra, Australia.

⁵ Institute for the Physics and Mathematics of the Universe, University of Tokyo, 5-1-5 Kashiwa-no-ha, Kashiwa, Chiba 277-8568, Japan.

June 11, 2010

ABSTRACT

Aims. We investigate the stellar kinematics and line strength indices in the outer halos of brightest cluster galaxies (BCGs) in the Coma cluster to obtain the outer halo V_{rot} and σ profiles and to derive constraints on the formation history of these objects.

Methods. We analyzed absorption lines in deep, medium-resolution, long-slit spectra in the wavelength range $\sim 4500 - 5900 \text{ \AA}$, out to $\sim 50 \text{ kpc}$ for NGC 4874 and $\sim 65 \text{ kpc}$ for NGC 4889, probing regions with a surface brightness down to $\mu_R \sim 24 \text{ mag arcsec}^{-2}$.

Results. These data provide stellar velocity and velocity dispersion profiles along the major axes of both BCGs, and also along the minor axis of NGC 4889. The kinematic properties of NGC 4874 and NGC 4889 halos extend the previous relations of early-type galaxy halos to bright luminosities and indicate that the stars in the outer regions are still bound to these galaxies. For NGC 4889 we also determine $H\beta$, Mg and Fe line strength indices, finding strong radial gradients for Mg and Fe. The current dataset for NGC 4889 is one of the most extended in radius, including both stellar kinematics and line strength index measurements.

Key words. galaxies: cluster: general – galaxies: cluster: individual: Coma cluster – galaxies: individual: NGC 4874 and NGC 4889 – galaxies: kinematics and dynamics – Galaxies: abundances

1. Introduction

Brightest cluster galaxies (BCGs) are large and luminous galaxies located in the centers of galaxy clusters. The formation history of BCGs and their halos is connected to the formation of the cluster itself (Dubinski 1998) and to the presence of diffuse intra-cluster light (Gonzalez et al. 2005; Murante et al. 2007). The formation of BCG and their halos can be investigated by the combined study of the stellar kinematics and the population content of their halos. Dynamical timescales in the halos are on the order of 1 Gyr^{-1} , approaching a significant fraction of the age of the universe, and therefore the fingerprints of the formation processes may still be preserved there.

So far, the studies that provide both stellar kinematics and line strength indices in BCGs have been limited to within one effective radius (e.g. Carter et al. 1999; Fisher et al. 1995; Brough et al. 2007; Spolaor et al. 2008a,b; Loubser et al. 2008, 2009), therefore measurements over a wider radial range are highly desirable.

This work is the first of a series aimed at studying the formation history of BCGs by probing the stellar kinematics and populations of their outer halos, covering regions at 3 effective radii or larger. As first targets, we selected NGC 4874 and NGC 4889, the two BCGs in the Coma cluster (Abell 1656). The in-

ner parts of these galaxies have been studied with photometric, kinematic and stellar populations data documented and available in the literature (e.g. Mehlert et al. 2000; Gavazzi et al. 2003; Gerhard et al. 2007; Trager et al. 2008).

In this paper we describe the data acquisition, reduction, and the measurements of the long slit stellar kinematics for both galaxies, and the line strength indices for NGC 4889. The data set in NGC 4889 extends out to 65 kpc (which correspond to ~ 4.3 effective radii, Jorgensen et al. 1995), providing the most radially extended measurements of absorption line kinematics and line strength indices in the outer halo of a BCG. These data are the basis of forthcoming papers investigating the formation history and evolution of the galaxies in the Coma cluster core.

The paper is organized as follows. Spectroscopic observations and data reduction are discussed in Section 2. The sky subtraction and the radial binning of the spectra are described in Sections 3 and 4, respectively. Section 5 describes the measurements of the stellar kinematics, while Section 6 describes the measurements of the line strength indices. Finally, the results are discussed in Section 7.

In this paper, we adopt a distance to NGC 4874 of $D = 102.6 \text{ Mpc}$ and an effective radius of $R_e = 70''.79 = 35.21 \text{ kpc}$; for NGC 4889 we adopt $D = 92.7 \text{ Mpc}$ and $R_e = 33''.88 = 15.23 \text{ kpc}$. Distances are taken from the NASA/IPAC Extragalactic Database (NED) and the effective radii from Jorgensen et al. (1995).

Send offprint requests to: L. Coccato, e-mail: lcoccato@mpe.mpg.de

[★] Based on data collected at Subaru Telescope, which is operated by the National Astronomical Observatory of Japan.

¹ Estimated for distance $R = 50 \text{ kpc}$ and circular velocity $V_c = 250 \text{ km s}^{-1}$, e.g. Binney & Tremaine 1987.

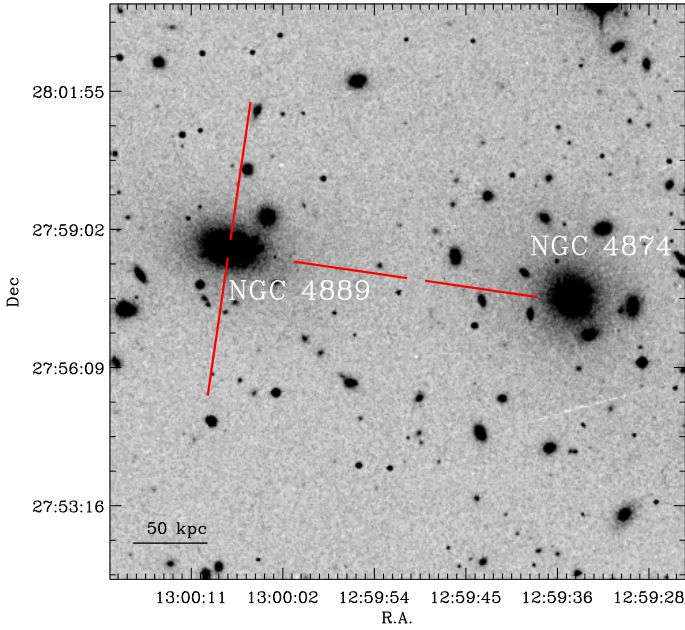


Fig. 1. Optical DSS image of the Coma cluster core. North is up, East is Left. The two red lines with the central gap represent the portion of the slit covered by the 2 CCDs in the FOCAS spectrograph. The scale in kpc given on the bottom left corner is computed assuming a distance of 97.7 Mpc, which is the average of the distances to NGC 4889 and NGC 4874 as given by NED.

2. Spectroscopic observations and data reduction

Long slit spectra were acquired with the Faint Object Camera And Spectrograph (FOCAS, Kashikawa et al. 2002) at the SUBARU telescope of the National Astronomical Observatory of Japan (NAOJ), on Mauna Kea (Hawaii, USA). Data were collected during two runs; in run #1 (April 2007) we obtained 8 hours integration long slit data on the West side of the NGC 4889 major axis, in the region in between NGC 4874 and NGC 4889, with a spectral resolution of 76 km s^{-1} . In run #2 (May 2008) we obtained 5.5 hours integration of long slit data for the NGC 4889 minor axis, with a spectral resolution of 96 km s^{-1} . In Figure 1 the observed field and slits locations are shown. In Table 1 we provide a summary of the observing log and instrumental set up. During these runs, we observed a set of kinematic template stars and Lick spectrophotometric standard stars for calibration to the Lick system. Long slit spectra on blank fields of the COMA cluster were also obtained for the sky background evaluation and to correct for large-scale illumination patterns due to slit vignetting. In addition, we observed at least one flux standard star per night, to flux calibrate the spectra.

Standard data reduction (bias subtraction, flat fielding to correct for pixel to pixel chip sensitivity fluctuations) were performed using standard IRAF² routines. Spectra distortion due to the optics were corrected using FOCASRED³ data reduction package within the IRAF environment. Cosmic rays were detected and removed using LACOS (van Dokkum 2001). Residual cosmic rays were removed by manually editing the spectrum. Wavelength calibration was performed using standard IRAF rou-

Table 1. Summary of the observing log and instrumental set up.

Parameter	Run 1 13-14 Apr. 2007	Run 2 8-9 May. 2008
Exp. time on galaxy	$16 \times 30 \text{ min}$	$11 \times 30 \text{ min}$
Exp. time on sky	$6 \times 30 \text{ min}$	$4 \times 10 \text{ min}$
Mean Seeing	$\sim 2''$	$\sim 2''$
R.A. slit center	12:59:51	13:00:08
DEC. slit center	+27:58:01	+27:58:37
Slit P.A.	$81^\circ 7'$	$-8^\circ 3'$
Slit length	300 arcsec	300 arcsec
Slit width	0.8 arcsec	1.0 arcsec
CCDs	MIT 2.2K \times 4K	MIT 2.2K \times 4K
Gain	$2.1 \text{ e}^- / \text{ADU}$	$2.1 \text{ e}^- / \text{ADU}$
R.O.N.	$4 \text{ e}^- \text{ rms}$	$4 \text{ e}^- \text{ rms}$
Pixel size	$15 \mu\text{m}$	$15 \mu\text{m}$
Pixel binning	3×1	3×1
Pixel scale	$0''.104 \text{ pixel}^{-1} (\times 3)$	$0''.104 \text{ pixel}^{-1} (\times 3)$
Grism	VPH 450	VPH 520
Filter	L600	L600
Dispersion	$0.394 \text{ \AA pixel}^{-1} (\times 1)$	$0.400 \text{ \AA pixel}^{-1} (\times 1)$
Observed range	4200 – 5700 \AA	4450 – 6050 \AA
Calibrated range	4545 – 5665 \AA	4700 – 5900 \AA
Calibration lamp	Th + Ar	Th + Ar
Instrumental $\sigma^{(*)}$	76 km s^{-1}	96 km s^{-1}

Notes – (*) Computed at 5100 \AA .

tines. Comparison Th+Ar spectra were obtained during the night close in time to the scientific spectra. Because two different grisms were used for the two runs, we optimized the wavelength calibration in different spectral ranges: $4545 \text{\AA} < \lambda < 5665 \text{\AA}$, for run 1, and $4700 \text{\AA} < \lambda < 5900 \text{\AA}$, for run 2. With this choice, we were able to minimize the errors in the wavelength calibration, which are about $\pm 10 \text{ km s}^{-1}$ as measured from the calibrated comparison spectra and from the sky line emission lines. Absorption lines as H β , Mg I($\lambda\lambda 5167, 5173, 5184$) triplet and Fe I($\lambda\lambda 5270, 5328$) fall inside the two selected wavelength ranges. Finally, the spectra were corrected for change in the slit illumination along the slit direction using the spectra obtained on sky blank fields.

3. Sky subtraction

Sky subtraction may introduce errors in the measurements from spectra of low surface brightness regions. To limit systematic effects as much as possible, we account for the sky subtraction in two ways.

The first method is to obtain sky spectra from blank fields. The sky spectrum is then free of contamination either from the galaxy halos or intracluster light, but the spectra are not taken simultaneously with the scientific exposures. Therefore, if the relative intensities of the sky continuum, emission or absorption lines change with time, sky residuals are present in the galaxy spectra.

The second method is to extract the sky spectrum from a region of the slit where the galaxy light is negligible (central part of the slit for run 1, outer borders of the slit for run 2). The sky is now observed simultaneously to the galaxy observations but the disadvantage is that it might contain a residual contribution from the galaxy halo and/or intracluster light. We then may subtract spectral features, which belong to the galaxy and which we are, in fact, interested in measuring.

² IRAF is distributed by NOAO, which is operated by AURA Inc., under contract with the National Science Foundation.

³ Information about the FOCASRED package can be obtained at the web page: <http://www.naoj.org/Observing/Instruments/FOCAS/Detail/UsersGuide/DataReduction/focasred.html>

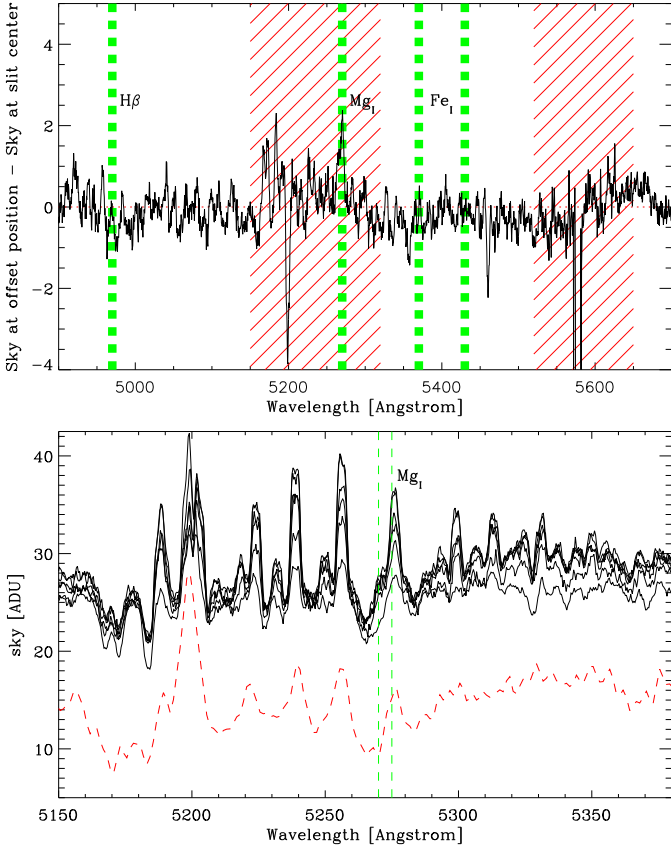


Fig. 2. *Upper panel:* difference between the mean sky spectrum measured at the offset position on the blank field and the sky spectrum measured at the long-slit center (run 1). The mean value of the difference is ≤ 1 ADU. The positions where galaxy absorption line features should be visible (taking into account the galaxy radial velocity) are marked in green (see text for details). The spectral ranges containing the most intense sky emission lines are shaded in red. *Lower panel:* comparison of sky spectra obtained at different times during the night (*black continuous lines*). The time variation of the relative intensity of sky emission and absorption lines is clearly visible. As in the upper panel, the position of the galaxy Mg I absorption line is marked in green. **For** comparison, we show also the typical sky spectrum visible from the Kitt Peak National Observatory (*red dashed line*, rescaled to allow comparison, from Massey & Foltz 2000). The same OH emission lines are visible.

In the upper panel of Fig. 2 we compare the sky spectra extracted using the two different methods. If the sky spectrum extracted at the slit center (run 1) or at the slit edges (run 2) contains a small residual contribution from the galaxy (stellar continuum and/or absorption line features) it should become visible when comparing with the sky spectrum extracted at the offset position. Residuals are approximately ± 0.5 counts (i.e. $\sim 2\%$ of the average sky level at 5100 Å). This means that the level of the sky continuum computed with the two methods is the same, and differences between the two methods (if any) should be associated with spectral line features. However, we clearly see that larger residuals are present in the wavelength regions of the most intense sky lines. In particular, a residual spectral feature is seen around ~ 5280 Å which is very close to the position of the Mg I($\lambda\lambda 5167, 5173, 5184$) triplet for the systemic velocity of NGC 4889. In the lower panel of Fig. 2 we

compare the sky spectra extracted at offset position at different times during the night. We concentrate on the spectral region from 5150 Å to 5380 Å, which contains some OH emission lines (Osterbrock et al. 1996). The variation of sky lines intensities over time is clearly visible and its amplitude ($\sim 1 - 2$ AUDs) is consistent with the intensity of the spectral feature observed at ~ 5280 Å. These time variations indicate that the observed residual at ~ 5280 Å is related to the sky and can be best corrected for by using the sky observed simultaneously to the scientific observations.

4. Extraction of spectra in low surface brightness regions

Before measuring the stellar kinematics (Section 5) and the line-strength indices (Section 6), we needed to bin spatially the spectra along the slit direction to increment the signal to noise ratio. Spectra from adjacent columns⁴ were added in order to reach a minimum signal to noise $S/N \sim 10$ for run 1, and $S/N \sim 20$ for run 2, which ensure reliable measurements of stellar kinematics and line strength indices. For run 1, the extracted spectra have an overall lower S/N than run 2 because the slit was sampling regions of lower surface brightness, and was illuminating regions of the CCD with bad cosmetics and hot columns which required masking.

Summing adjacent spectra over part of the slit may affect the absorption line shapes by either smoothing the intrinsic velocity gradient or enlarging the absorption lines, if there is a substantial velocity gradient in the sampled region.

Such an effect may be significant for run 1, where the slit sampled halo light of galaxies whose systemic velocities differ by ~ 700 km s⁻¹. We estimated the maximum number of adjacent columns to be summed and extracted in a one-dimensional spectrum to be approximately $\sim 30 - 40$, depending also on the CCD cosmetics. Within this range, the maximum smoothing of the intrinsic velocity gradient is approximately $\sim 20 - 30$ km s⁻¹, which is the same order as the measurement errors. This value is obtained multiplying the number of columns by the maximum velocity gradient along the slit⁵, which we estimated to be ~ 0.8 km s⁻¹ pixel⁻¹. For run 2, we estimated the effect to be negligible, because no velocity gradient was measured along the minor axis of NGC 4889 (Section 5).

In the case of NGC 4874, the 1D spectra obtained from 40 adjacent columns did not reach the required S/N . For those regions we used the following iterative procedure:

1. We selected N regions on the slit which are $M \leq 30$ pixels wide. Each region corresponds to a two-dimensional spectrum, which we call “stripe” S_i (with $i = 1, \dots, N$). Each of the N stripes is composed of M one-dimensional adjacent spectra, with the wavelength direction oriented along columns.
2. We extracted the one-dimensional spectrum S_i^C , by summing the stripe along the slit direction, and assigned the luminosity weighted central position R_i (in pixels) on the slit. We associated thus a spectrum S_i^C and a central position R_i^C to each region of the slit.

⁴ The spectra were oriented to have the dispersion direction along the vertical axis, and the slit aligned with the horizontal axis.

⁵ This gradient was computed from the velocity difference measured at the slit edges (~ 800 km s⁻¹) divided by the number of pixels in the slit (960).

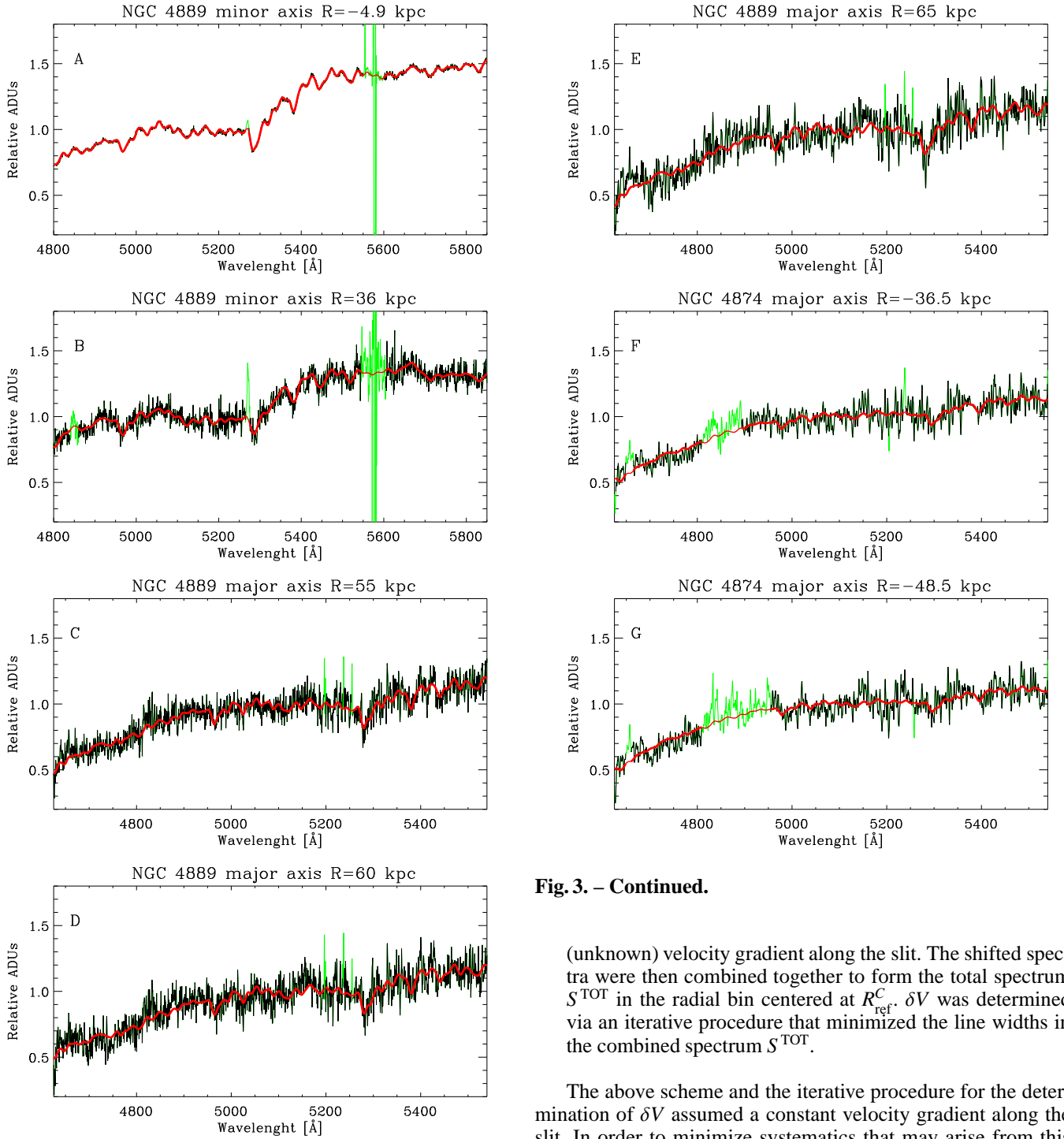


Fig. 3. Examples of kinematic fits. *Black*: galaxy spectrum, *green*: portion of galaxy spectrum excluded in the fit, *red*: best fit template model. The S/N ratio per pixel of the spectra in panels from A to G are: 61, 15, 13, 10, 9, 8, 8, respectively. All spectra are normalized to the value of the best fit model at 5100 Å.

3. We measured the radial velocity V_i^C of the spectrum S_i^C . The radial velocity measurements are described in Section 5.
4. We selected a reference spectrum S_{ref}^C . The other $N - 1$ spectra were then shifted to the radial velocity V_{ref}^C of the reference spectrum. The ΔV applied to the $S_{i\text{-th}}^C$ spectrum was $\Delta V = \delta V \cdot (R_i^C - R_{\text{ref}}^C)$, where δV (in $\text{km s}^{-1} \text{ pixel}^{-1}$) is the

Fig. 3. – Continued.

(unknown) velocity gradient along the slit. The shifted spectra were then combined together to form the total spectrum S^{TOT} in the radial bin centered at R_{ref}^C . δV was determined via an iterative procedure that minimized the line widths in the combined spectrum S^{TOT} .

The above scheme and the iterative procedure for the determination of δV assumed a constant velocity gradient along the slit. In order to minimize systematics that may arise from this assumption, we limited the radial binning to a maximum of 3 adjacent stripes $S_{i-1,i,i+1}$, each of them 30 pixels wide at most.

5. Stellar kinematics

Stellar kinematics from the extracted spectra in the radial bins were measured using the “Penalized Pixel-Fitting method” (PPXF, Cappellari & Emsellem 2004). A library of kinematic template stars (MILES library, Sánchez-Blázquez et al. 2006) was used together with stellar templates observed during the observations. The template spectra of the MILES library were convolved with a Gaussian function to match the FOCAS spectral resolution. We show some of the fit results in Figure 3: the innermost and outermost spectra extracted along the minor axis of

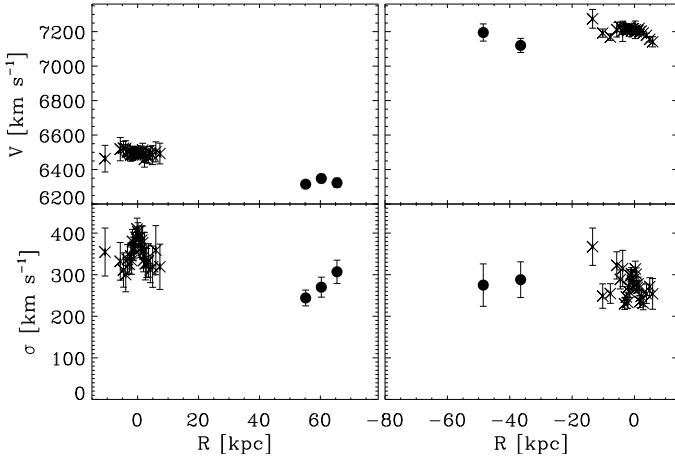


Fig. 4. Radial velocity (*upper panels*) and velocity dispersion profiles (*lower panels*) along the slit in run 1 (velocities are expressed in the heliocentric reference system). Measurements along the slit are divided in two panels, with *left panels* referring to the part of the slit close to NGC 4889 and *right panels* referring to the part of the slit close to NGC 4874. *Crosses*: data from Mehlert et al. (2000) shifted to the systemic velocities, 6495 km s⁻¹ for NGC 4889 (Moore et al. 2002) and 7205 km s⁻¹ for NGC 4874 (Smith et al. 2004). *Filled circles*: measurements from this paper for run 1.

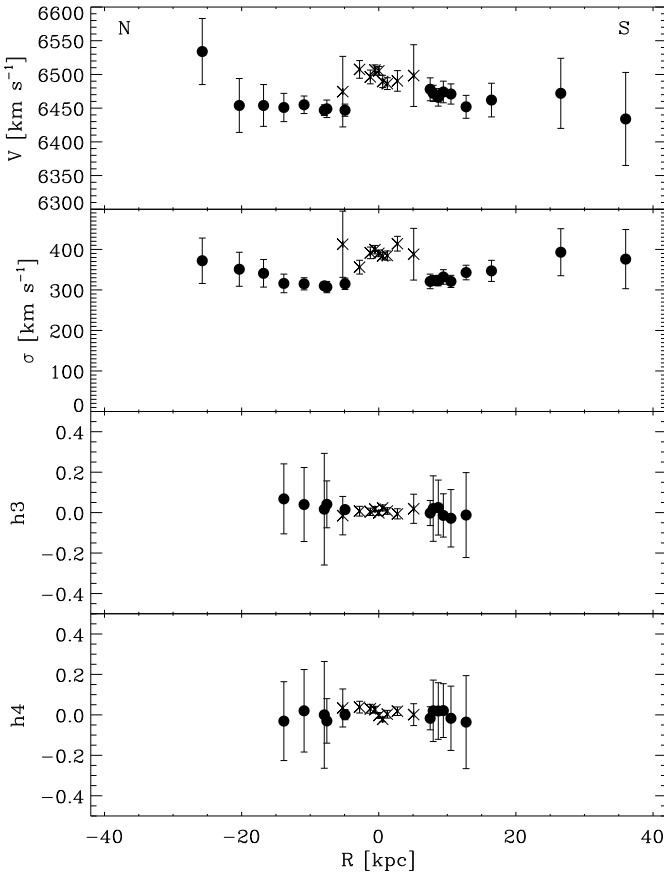


Fig. 5. Stellar kinematics along the minor axis of NGC 4889. *Crosses*: data from Corsini et al. (2008), *filled circles*: measurements from this paper for run 2.

NGC 4889, the three outermost spectra along the major axis of NGC 4889 and the two spectra of NGC 4874 are also shown.

The wavelength ranges used for the fitting are $4600\text{\AA} < \lambda < 5550\text{\AA}$ for run 1, and $4800\text{\AA} < \lambda < 5850\text{\AA}$ for run 2. Bad pixels coming from residual cosmic rays or emission lines were properly masked and not included in the fitting procedure.

For each radial bin, the PPXF code built the optimal template which represents the observed spectrum by a linear combination of different stellar templates. The use of a large spectral library and the creation of one optimal template for each radial bin minimized errors in the kinematics due to template mismatch. In the outermost bins ($R \geq 60$ kpc in run 1 and $|R| > 20$ kpc in run 2) the construction of the optimal stellar template in PPXF failed, because the absorption line features are less pronounced. The kinematics in these regions were measured using the best template obtained from the nearest bin in which it could be obtained. Referring to Fig. 3, spectra in panels D, E, F and G were fitted using the optimal template determined when fitting the spectrum in panel C. The spectrum in panel B was fitted with the optimal template obtained fitting the spectrum at 16 kpc (not shown in the figure). This approximation might introduce some systematic errors in the kinematics of the outer bins due to template mismatch. Nevertheless, in the radial bins ($|R| \leq 20$ kpc in run 2), we did not observe significant differences in the kinematics when either the “central” optimal template at $R = -4.9$ kpc or the “local” optimal templates, found by PPXF for those bins, were used. This confirmed that errors on the kinematics caused by template mismatch were negligible for the inner bins, and gave us confidence that the template mismatch is not important in the outer bins. Errors on the measured kinematics were determined by means of Monte Carlo simulations, analyzing spectra generated from the best fit template model and adding the appropriate noise.

The measured radial velocities were then shifted to the heliocentric reference system using the MIDAS⁶ task COMPUT/BARY.

The fitted mean velocity, velocity dispersion and Gauss-Hermite moments (Gerhard 1993; van der Marel & Franx 1993) and their errors are shown in Figures 4 and 5 for runs 1 and 2, respectively, and are listed in Table 2. Gauss-Hermite moments were fitted only for spectra within $|R| < 20$ kpc along the minor axis.

6. Line strength indices

Line strength indices were measured for NGC 4889 using observations from both runs. The spectra of NGC 4874 did not have enough S/N for this. We measured the $H\beta$, Mg_1 , Mg_2 , $Mg\ b$, $Fe5270$ and $Fe5335$ line-strength indices as defined by Faber et al. (1985) and Worthey et al. (1994). The spectra were convolved with a Gaussian function to match the spectral resolution of the Lick system ($FWHM = 8.4\text{\AA}$ at 5100\AA , Worthey & Ottaviani 1997). Three Lick standard stars observed during the runs were used to correct for offsets to the Lick system. The measured offsets (FOCAS - Lick) are: 0.03\AA ($H\beta$), -0.30\AA ($Fe5105$), -0.028 mag (Mg_1), -0.016 mag (Mg_2), -0.037\AA ($Mg\ b$), -0.36\AA ($Fe5270$), 0.024\AA ($Fe5335$) and 0.024\AA ($Fe5406$).

No focus correction was applied because atmospheric seeing was the dominant effect during observations.

⁶ MIDAS is developed and maintained by the European Southern Observatory.

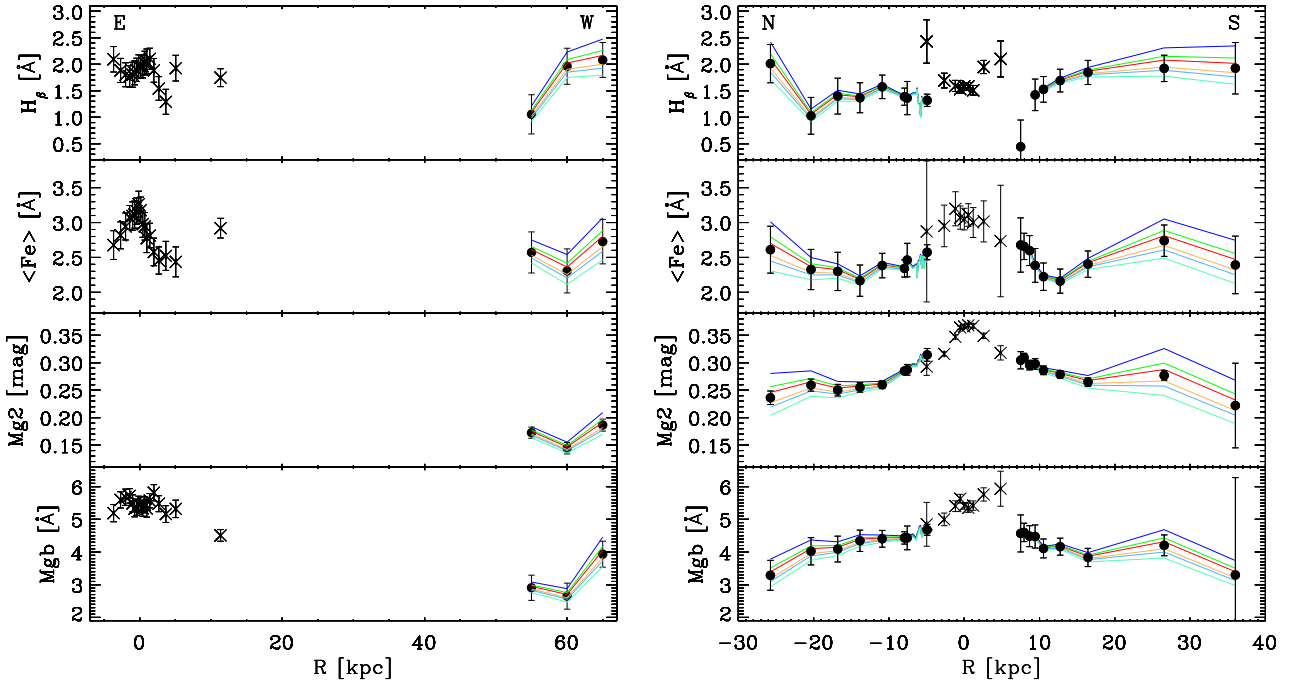


Fig. 6. Line-strength Lick indices for NGC 4889 measured along the major (*left panel*) and the minor axis (*right panel*). Crosses: data from Mehlert et al. 2000 (major axis) and Corsini et al. 2008 (minor axis). *Filled circles*: measurements from this paper. *Solid lines* indicate the systematic deviations of the line-strength measurements caused by adding different residual sky levels to the extracted galaxy spectrum. From top to bottom, the residual sky levels we added are +2% (i.e. sky subtraction is underestimated by 2%), +1%, +0.5%, -0.5%, -1%, -2% (i.e. sky subtraction overestimated by 2%). See Section 3 for details.

Errors on line-strength indices were determined via Monte Carlo simulations, which accounted for the errors on radial velocity measurement also. Errors from Monte Carlo simulations are consistent with those predicted by the analytic formulae of Cardiel et al. (1998).

In the following we describe the details of additional corrections we applied to the measurements in order to take into account instrumental effects. The final measured values are listed in Table 2 and are shown in Figure 6 together with the Mehlert et al. (2000) data along the major axis, and the Corsini et al. (2008) data along the minor axis⁷.

6.1. Correction for intrinsic broadening

The line-strength measurements were corrected for the galaxy intrinsic broadening following the procedure described in Kuntschner et al. (2006). Coefficients C_I for each index I were determined as the ratio of i) the “intrinsic” values (I_0 , in Angstrom) measured on the optimal stellar template; and ii) the line-of-sight-velocity-distribution “modified” values (I_{LOSVD}) measured on the best fit model (i.e. the optimal template convolved with the galaxy LOSVD). Corrected galaxy line strength indices (in Angstrom) were then given by:

$$I_{\text{corr}} = C_I \cdot I_{\text{meas}} = \frac{I_0}{I_{\text{LOSVD}}} \cdot I_{\text{meas}} \quad (1)$$

⁷ We show the mean iron $\langle \text{Fe} \rangle = \frac{1}{2} (\text{Fe}5270 + \text{Fe}5335)$ radial profiles and not the profiles of both iron indices to facilitate the comparison with the literature, **where** only $\langle \text{Fe} \rangle$ is provided.

6.2. Correction for residual emission lines

The long-slit spectra for the NGC 4889 minor axis showed strong unresolved emission lines in the wavelength regions adjacent to the MgI bandpass and the $\text{H}\beta$ blue pseudo-continuum. These strong lines were at wavelengths that are not associated with known galaxy emission lines or sky/auroral lines. Our conclusion was that they may be associated with internal reflections in the spectrograph. To measure the spectral indices in the regions affected by the unidentified emission lines, we simultaneously fit the galaxy spectrum with a stellar template plus Gaussian functions at the wavelength of the detected emissions. The best-fit Gaussians were then subtracted from the spectrum, to remove the observed emission lines. As a further test, we checked the measured values of the line-strength indices against the measurements on the best-fit stellar template, convolved with the galaxy line of sight velocity distribution determined in Section 5. The two sets of values were consistent.

6.3. Systematic effects caused by sky subtraction

We then quantified the systematic errors in the line strength indices measurements caused by sky subtraction. A residual sky contribution of $\pm 0.5\%$, $\pm 1\%$ and $\pm 2\%$ of the subtracted sky spectrum⁸ was added to the extracted galaxy spectra, and then we performed measurements of the line-strength indices on these modified spectra. Within the errorbars, these new values were consistent with the measurements performed on the best back-

⁸ Residual sky contribution larger than 2% would produce detectable sky features either in emission or absorption in the galaxy spectra. 2% is also the maximum difference between the continuum of the sky measured at blank fields and the one measured simultaneously to galaxy observations (see Section 3 and Fig. 2 for discussion).

ground subtracted galaxy spectra, but for the Mg_2 index. This was probably due to the fact that the Mg_2 pseudo-continua were defined on spectral regions not adjacent to the index passband (unlike for the other spectral indices), therefore variations of the sky level have a larger effect on this index.

7. Results and discussion

In NGC 4874 the measured stellar kinematics extend out to ~ 50 kpc ($\sim 1.4R_e$) along its East side. Measurements of line strength indices were not possible.

In NGC 4889 our measurements extend out to 65 kpc ($\sim 4.3R_e$) along its West side (close to its major axis) and ~ 35 kpc ($\sim 2.3R_e$) along its photometric minor axis. This represents the most spatially extended datasets with both stellar kinematics *and* line strength indices for a brightest cluster galaxy.

7.1. Kinematics

NGC 4874. In NGC 4874 the outer mean velocity along the line of sight is $\langle V \rangle = 7150 \pm 37 \text{ km s}^{-1}$, about $\sim 55 \text{ km s}^{-1}$ lower than the galaxy systemic velocity ($V_{\text{sys}} = 7205 \pm 19 \text{ km s}^{-1}$, as reported by Smith et al. 2004). It is not straightforward to associate it with rotation or tidal effects, given the errors on the current measurements and the large uncertainties on the galaxy systemic velocity. As examples, de Vaucouleurs et al. (1991, RC3 hereafter) report a systemic velocity of $7152 \pm 16 \text{ km s}^{-1}$, while NED reports a systemic velocity of $7224 \pm 11 \text{ km s}^{-1}$. The mean outer velocity dispersion in NGC 4874 is $\sigma = 283 \pm 33 \text{ km s}^{-1}$, which is consistent with the central value found by Smith et al. (2004), suggesting a flat velocity dispersion profile with radius.

NGC 4889. In NGC 4889 the mean outer velocity is $\langle V \rangle = 6326 \pm 44 \text{ km s}^{-1}$, which is $\sim 169 \text{ km s}^{-1}$ lower than the galaxy systemic velocity ($V_{\text{sys}} = 6495 \pm 13 \text{ km s}^{-1}$, as reported by Moore et al. 2002). The measured velocity offset is significant when compared with measurements errors and uncertainties on the systemic velocity. Although rotation in the halos of ellipticals is not rare (e.g. Rix et al. 1999; Coccato et al. 2009), it is not straightforward to consider the velocity offset as evidence of rotation, since we miss measurements on the East side of the galaxy. The outer mean velocity dispersion we measured in NGC 4889 is $\sigma = 266 \pm 17 \text{ km s}^{-1}$, consistent with the outermost measurements ($\sim 10''$) by Moore et al. (2002), revealing a flat velocity dispersion profile outside the central drop.

Gerhard et al. (2007) developed a model for the core of the Coma cluster whereby the two BCGs, NGC 4874 and NGC 4889, are in the process of merging, tidally stripping each others' halos to create an elongated distribution of intracluster light in which they are embedded. It is worth noting that, out to the radii probed by the present observations, the velocity dispersion profiles of NGC 4874 and NGC 4889 are nearly constant and indicative of stars still bound to the central galaxy. This is consistent with recent velocity dispersion profiles measurements based on planetary nebulae and globular clusters for local brightest cluster galaxies (e.g. Coccato et al. 2009; Doherty et al. 2009; Proctor et al. 2009; Schubert et al. 2009; McNeil et al. 2010 A&A submitted). These galaxies do not show an increase in the velocity dispersion profile as observed in other BCGs (e.g. NGC 6166 in Kelson et al. 2002), which was interpreted as generated by stars not bound to the galaxy but free floating in the cluster potential.

We can thus compare the kinematic properties of the outer regions of NGC 4874 and NGC 4889 with the kinematic properties of the outer halos of other early-type galaxies. To do this, we

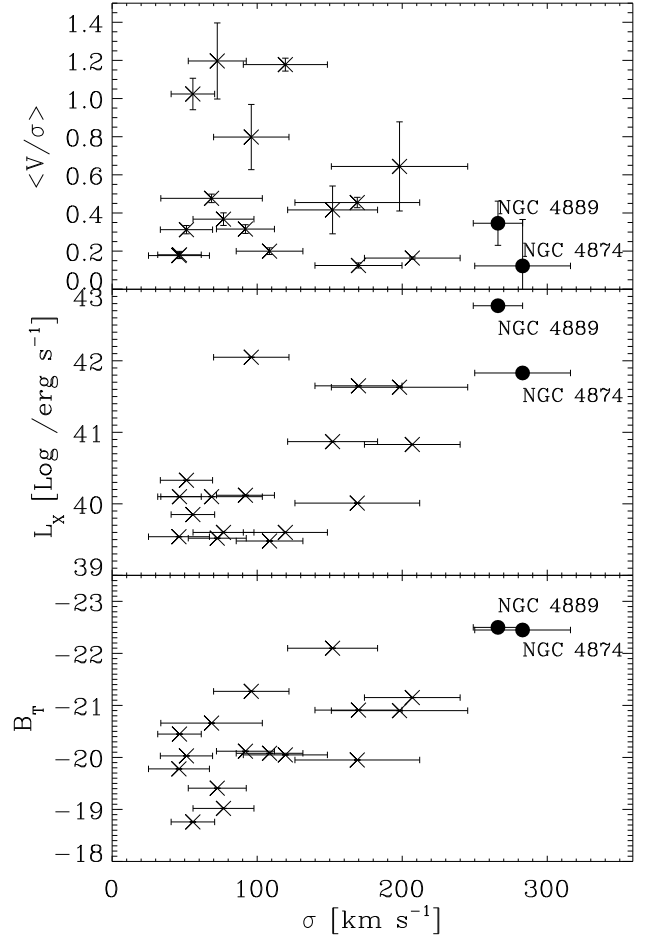


Fig. 7. Correlations between the outermost measured value of the halo velocity dispersion and mean $\langle V/\sigma \rangle$ of the halo (*upper panel*), total X-ray luminosity (*central panel*) and total luminosity in the B band (*lower panel*). Crosses are data from Coccato et al. (2009), filled circles are data from this paper.

refer to the results of Coccato et al. (2009) based on radial velocities of Planetary Nebulae in the halos of early-type galaxies. Their sample covers the range $50 \text{ km s}^{-1} \lesssim \sigma \lesssim 220 \text{ km s}^{-1}$ of velocity dispersion in the outer halo. The two galaxies studied in this paper fall in the upper σ range of the galaxy sample explored by Coccato et al. 2009 and this enables us to extend their σ range. Following Coccato et al. (2009), in Figure 7 we compare the halo velocity dispersion with other galaxy properties, $\langle V/\sigma \rangle$ (we assume that the observed velocity offset is due to rotation), total X-ray luminosity ($L_X = 6.8 \cdot 10^{41} \text{ erg s}^{-1}$ for NGC 4874 and $L_X = 5.9 \cdot 10^{42} \text{ erg s}^{-1}$ for NGC 4889, from Pellegrini 2005) and total B-band magnitude ($B_T = -22.45$ for NGC 4874 and $B_T = -22.50$ for NGC 4889, from RC3). Both NGC 4874 and NGC 4889 follow the same trend found in other early-type galaxies, therefore supporting the earlier statement that the stars in their halos are still bound to the inner galaxies in the radial range explored in this work.

7.2. Line strength indices

In NGC 4889, the measured set of Lick indices provides information in the radial interval from ~ 7 to ~ 65 kpc, and is comple-

mentary to data available for the central regions (Mehlert et al. 2000; Corsini et al. 2008).

In the region of overlap the current data set and the published values agree along the minor axis ($|R| \sim 5$ kpc), but for $H\beta$.

In the central parts of the galaxy, the mean value from Corsini et al. (2008) data is higher than the inward extrapolation of our data by 0.3 \AA . Their outermost central value differs from ours of 1.1 \AA at the same radius ($R \sim -5$ kpc, see Fig. 6).

The difference could be related either to the limited number of stars we used to correct the FOCAS observations to the Lick system, or to sky subtraction, affecting Corsini's measurements (see Section 6). But in these cases we would expect a discrepancy also in other indices, and not only in $H\beta$. Another reason could be the presence of emission lines, but neither in our spectra nor in Corsini's spectra $H\beta$ emission lines were detected at 5 kpc. Therefore, the reason for the discrepancy remains unclear.

Values of $H\beta$ range from 0.5 to 2.3 \AA . Line strength indices related to $Mg \text{ I}$ and $< Fe >$ show declining profiles, from the central values of $Mg_2 \sim 0.37 \text{ \AA}$, $Mg \text{ b} \sim 5.5 \text{ \AA}$ and $< Fe > \sim 3.4 \text{ \AA}$, to outer values of $Mg_2 \sim 0.15 \text{ \AA}$, $Mg \text{ b} \sim 3 \text{ \AA}$ and $< Fe > \sim 2.5 \text{ \AA}$.

In Coccato et al. (2010) the combined set of line strength indices for NGC 4889 is used to derive age, metallicity and alpha-enhancement for single stellar population models and their radial gradients from the center out to 60 kpc. There we find evidence for a change in the stellar population gradient and content, suggesting a different evolutionary history between the galaxy and its halo. We refer to this forthcoming paper for a detailed discussion of the implications of these measurements for the properties of the stellar populations in NGC 4889, and for the constraints they put on the galaxy formation mechanism.

Acknowledgements. The authors wish to thank T. Hattori for the professional support during the observations and for providing the FOCASRED package used in the data reduction; R. Bender, E. Iodice, H. Kuntschner, L. Morelli, R.P. Saglia, D. Thomas and J. Thomas for useful discussions.

This research has made use of the NASA/IPAC Extragalactic Database (NED) which is operated by the Jet Propulsion Laboratory, California Institute of Technology, under contract with the National Aeronautics and Space Administration, and of the "Penalized Pixel-Fitting method" by Cappellari & Emsellem (2004).

References

- Binney, J. & Tremaine, S. 1987, Galactic dynamics (Princeton, NJ, Princeton University Press, 1987, 747 p.)
- Brough, S., Proctor, R., Forbes, D. A., et al. 2007, MNRAS, 378, 1507
- Cappellari, M. & Emsellem, E. 2004, PASP, 116, 138
- Cardiel, N., Gorgas, J., Cenarro, J., & Gonzalez, J. J. 1998, A&AS, 127, 597
- Carter, D., Bridges, T. J., & Hau, G. K. T. 1999, MNRAS, 307, 131
- Coccato, L., Gerhard, O., & Arnaboldi, M. 2010, MNRAS in press
- Coccato, L., Gerhard, O., Arnaboldi, M., et al. 2009, MNRAS, 394, 1249
- Corsini, E. M., Wegner, G., Saglia, R. P., et al. 2008, ApJS, 175, 462
- de Vaucouleurs, G., de Vaucouleurs, A., Corwin, Jr., H. G., et al. 1991, Third Reference Catalogue of Bright Galaxies (RC3)
- Doherty, M., Arnaboldi, M., Das, P., et al. 2009, A&A, 502, 771
- Dubinski, J. 1998, ApJ, 502, 141
- Faber, S. M., Friel, E. D., Burstein, D., & Gaskell, C. M. 1985, ApJS, 57, 711
- Fisher, D., Franx, M., & Illingworth, G. 1995, ApJ, 448, 119
- Gavazzi, G., Boselli, A., Donati, A., Franzetti, P., & Scodreggio, M. 2003, A&A, 400, 451
- Gerhard, O., Arnaboldi, M., Freeman, K. C., et al. 2007, A&A, 468, 815
- Gerhard, O. E. 1993, MNRAS, 265, 213
- Gonzalez, A. H., Zabludoff, A. I., & Zaritsky, D. 2005, ApJ, 618, 195
- Jorgensen, I., Franx, M., & Kjaergaard, P. 1995, MNRAS, 273, 1097
- Kashikawa, N., Aoki, K., Asai, R., et al. 2002, PASJ, 54, 819
- Kelson, D. D., Zabludoff, A. I., Williams, K. A., et al. 2002, ApJ, 576, 720
- Kuntschner, H., Emsellem, E., Bacon, R., et al. 2006, MNRAS, 369, 497
- Loubser, S. I., Sánchez-Blázquez, P., Sansom, A. E., & Soechting, I. K. 2009, MNRAS, 398, 133

- Loubser, S. I., Sansom, A. E., Sánchez-Blázquez, P., Soechting, I. K., & Bromage, G. E. 2008, MNRAS, 391, 1009
- Massey, P. & Foltz, C. B. 2000, PASP, 112, 566
- Mehlert, D., Saglia, R. P., Bender, R., & Wegner, G. 2000, A&AS, 141, 449
- Moore, S. A. W., Lucey, J. R., Kuntschner, H., & Colless, M. 2002, MNRAS, 336, 382
- Murante, G., Giovalli, M., Gerhard, O., et al. 2007, MNRAS, 377, 2
- Osterbrock, D. E., Fulbright, J. P., Martel, A. R., et al. 1996, PASP, 108, 277
- Pellegrini, S. 2005, MNRAS, 364, 169
- Proctor, R. N., Forbes, D. A., Romanowsky, A. J., et al. 2009, MNRAS, 398, 91
- Rix, H.-W., Carollo, C. M., & Freeman, K. 1999, ApJ, 513, L25
- Sánchez-Blázquez, P., Peletier, R. F., Jiménez-Vicente, J., et al. 2006, MNRAS, 371, 703
- Schuberth, Y., Richtler, T., Hilker, M., et al. 2009, ArXiv e-prints
- Smith, R. J., Hudson, M. J., Nelan, J. E., et al. 2004, AJ, 128, 1558
- Spolaor, M., Forbes, D. A., Hau, G. K. T., Proctor, R. N., & Brough, S. 2008a, MNRAS, 385, 667
- Spolaor, M., Forbes, D. A., Proctor, R. N., Hau, G. K. T., & Brough, S. 2008b, MNRAS, 385, 675
- Trager, S. C., Faber, S. M., & Dressler, A. 2008, MNRAS, 386, 715
- van der Marel, R. P. & Franx, M. 1993, ApJ, 407, 525
- van Dokkum, P. G. 2001, PASP, 113, 1420
- Worthey, G., Faber, S. M., Gonzalez, J. J., & Burstein, D. 1994, ApJS, 94, 687
- Worthey, G. & Ottaviani, D. L. 1997, ApJS, 111, 377

Table 2. Stellar kinematics and line strenght indices for NGC 4874 (run 1) and NGC 4889 (runs 1 and 2).

R (kpc) (1)	V_{\odot} (km s ⁻¹) (2)	σ (km s ⁻¹) (3)	h_3 (4)	h_4 (5)	H β (Å) (6)	Fe5105 (Å) (7)	Mg ₁ (mag) (8)	Mg ₂ (mag) (9)	Mg b (Å) (10)	Fe5270 (Å) (11)	Fe5335 (Å) (12)	Fe5406 (Å) (13)
Run1:												
N 4874												
-48.50	7195 ± 50	275 ± 51	–	–	–	–	–	–	–	–	–	–
-36.51	7120 ± 41	288 ± 43	–	–	–	–	–	–	–	–	–	–
N 4889												
55.17	6315 ± 18	244 ± 19	–	–	1.05 ± 0.37	–	0.05 ± 0.08	0.173 ± 0.010	2.91 ± 0.39	2.43 ± 0.38	2.71 ± 0.46	–
60.31	6348 ± 24	270 ± 24	–	–	1.96 ± 0.34	–	0.02 ± 0.09	0.144 ± 0.010	2.65 ± 0.40	2.12 ± 0.43	2.50 ± 0.46	–
65.46	6323 ± 27	307 ± 28	–	–	2.08 ^(*) ± 0.33	–	0.03 ± 0.09	0.186 ± 0.011	3.93 ± 0.40	2.81 ± 0.41	2.64 ± 0.50	–
Run2:												
N 4889												
-25.74	6534 ± 49	372 ± 56	–	–	2.01 ± 0.36	–	–	0.24 ^(*) ± 0.01	3.29 ^(*) ± 0.46	2.44 ± 0.46	2.78 ± 0.49	1.40 ± 0.46
-20.34	6454 ± 40	351 ± 42	–	–	1.03 ± 0.35	4.27 ± 0.87	–	0.26 ^(*) ± 0.01	4.02 ^(*) ± 0.42	2.38 ± 0.40	2.27 ± 0.42	1.32 ± 0.37
-16.80	6454 ± 31	341 ± 34	–	–	1.40 ± 0.34	3.80 ± 0.72	–	0.25 ^(*) ± 0.01	4.09 ^(*) ± 0.39	2.22 ± 0.38	2.38 ± 0.39	–
-13.84	6451 ± 21	316 ± 23	0.07 ± 0.17	-0.03 ± 0.20	1.37 ± 0.28	3.76 ± 0.70	0.16 ± 0.07	0.255 ± 0.009	4.34 ± 0.33	2.12 ± 0.31	2.21 ± 0.32	1.28 ± 0.33
-10.89	6455 ± 13	315 ± 15	0.04 ± 0.18	0.02 ± 0.20	1.57 ± 0.22	4.25 ± 0.58	0.17 ± 0.05	0.260 ± 0.007	4.41 ± 0.26	2.44 ± 0.24	2.33 ± 0.25	1.25 ± 0.27
-7.94	6447 ± 8	310 ± 9	0.02 ± 0.28	0.00 ± 0.26	1.39 ± 0.16	4.50 ± 0.46	0.18 ± 0.04	0.285 ± 0.005	4.43 ± 0.19	2.34 ± 0.17	2.34 ± 0.18	1.39 ± 0.21
-7.57	6449 ± 13	307 ± 14	0.04 ± 0.12	-0.03 ± 0.11	1.36 ± 0.31	4.53 ± 0.33	0.18 ± 0.08	0.287 ± 0.010	4.43 ± 0.36	2.42 ± 0.33	2.50 ± 0.35	1.44 ± 0.15
-4.92	6447 ± 9	315 ± 14	0.02 ± 0.02	0.00 ± 0.03	1.32 ± 0.12	4.89 ± 0.16	0.19 ± 0.11	0.314 ± 0.012	4.68 ± 0.17	2.62 ± 0.20	2.53 ± 0.13	1.57 ± 0.07
7.50	6478 ± 17	321 ± 18	-0.00 ± 0.06	-0.02 ± 0.06	0.44 ± 0.50	4.59 ± 0.51	0.19 ± 0.12	0.305 ± 0.016	4.57 ± 0.57	2.88 ± 0.53	2.47 ± 0.58	1.73 ± 0.24
7.94	6472 ± 12	323 ± 12	0.02 ± 0.16	0.02 ± 0.15	–	–	0.19 ± 0.06	0.309 ± 0.008	4.60 ± 0.28	2.66 ± 0.26	2.65 ± 0.28	1.73 ± 0.45
8.68	6466 ± 13	323 ± 13	0.03 ± 0.14	0.02 ± 0.14	–	4.67 ± 0.49	0.18 ± 0.07	0.296 ± 0.009	4.49 ± 0.32	2.55 ± 0.29	2.64 ± 0.31	1.77 ± 0.22
9.42	6474 ± 16	332 ± 18	-0.01 ± 0.11	0.02 ± 0.13	1.42 ± 0.30	4.90 ± 0.56	–	0.30 ^(*) ± 0.01	4.48 ^(*) ± 0.35	2.42 ± 0.33	2.36 ± 0.36	1.83 ± 0.25
10.53	6471 ± 15	321 ± 15	-0.03 ± 0.14	-0.02 ± 0.16	1.53 ± 0.24	4.48 ± 0.63	–	0.29 ^(*) ± 0.01	4.11 ^(*) ± 0.29	2.26 ± 0.27	2.19 ± 0.29	1.50 ± 0.28
12.74	6452 ± 17	343 ± 18	-0.01 ± 0.21	-0.04 ± 0.23	1.69 ± 0.21	4.76 ± 0.51	–	0.28 ^(*) ± 0.01	4.16 ^(*) ± 0.26	1.95 ± 0.24	2.37 ± 0.25	1.61 ± 0.23
16.44	6462 ± 25	347 ± 26	–	–	1.85 ± 0.23	4.61 ± 0.44	–	0.27 ^(*) ± 0.01	3.83 ^(*) ± 0.29	2.08 ± 0.26	2.73 ± 0.28	1.44 ± 0.21
26.55	6472 ± 52	393 ± 58	–	–	1.92 ± 0.25	–	–	0.28 ^(*) ± 0.01	4.20 ^(*) ± 0.32	2.03 ± 0.31	3.44 ± 0.33	1.56 ± 0.23
36.01	6434 ± 69	376 ± 73	–	–	1.92 ± 0.49	–	–	0.22 ^(*) ± 0.08	3.30 ^(*) ± 2.98	2.02 ± 0.57	2.77 ± 0.60	–

Notes – Measurements marked by ^(*) were obtained by removing an emission line component from the spectrum. The symbol – means that the measurement has not been performed.